Journal of Science and Transport Technology
Journal homepage: https://jstt.vn/index.php/en

Sliding mode control of a rotary double parallel inverted pendulum

Thanh-Tung Nguyen[1], Minh-Tai Vo[2], Van-Dong-Hai Nguyen[1,*]
[1]Ho Chi Minh City University of Technology and Engineering (HCM-UTE), Ho Chi Minh City 700000, Vietnam; 2341107@student.hcmute.edu.vn, hainvd@hcmute.edu.vn
[2]Posts and Telecommunications Institute of Technology, Ho Chi Minh City 700000, Vietnam; taivm@ptit.edu.vn

Article info
Type of article:
Original research paper

DOI:
https://doi.org/10.58845/jstt.utt.2026.en.6.1.314-332

***Corresponding author:**
Email address:
hainvd@hcmute.edu.vn

Received: 31/05/2025
Received in Revised Form: 16/02/2026
Accepted: 09/03/2026

Abstract: This study explores the stabilization of a rotating parallel inverted pendulum, a nonlinear, underactuated system challenging conventional control methods. Unlike prior work focusing on linear techniques like Linear Quadratic Regulator, which lack robustness to uncertainties, this research introduces a Sliding Mode Control (SMC) strategy. Utilizing a linear sliding surface, the proposed SMC ensures finite-time convergence and robust performance despite model uncertainties and disturbances. Numerical simulations and experimental results validate the controller's ability to stabilize the pendulum and rotating base, demonstrating its superiority over traditional methods and potential applicability to similar complex mechanical systems.

Keywords: Sliding mode control, Linear sliding mode control, Linear sliding surface, Rotary parallel inverted pendulum.

1. Introduction

The inverted pendulum has long been recognized as a classical benchmark for evaluating control strategies, owing to its underactuated structure, nonlinear dynamics, and strong inter-axis coupling. This system encapsulates core challenges in control engineering, including stabilization, disturbance rejection, and trajectory tracking, thereby making it an effective platform for theoretical validation and comparative assessment of control methodologies. Consequently, it has attracted considerable academic attention and has played a pivotal role in the evolution of modern control theory [1]-[4].

A recent extension of this model, the rotary parallel double inverted pendulum (RPDIP), is illustrated in Fig. 1. The RPDIP configuration introduces additional mechanical complexity and degrees of freedom, resulting in more intricate nonlinear behavior and tighter dynamic coupling.

These characteristics pose increased difficulty in both modeling and control. Research focused on the RPDIP is expected to provide valuable insights into the development of advanced control frameworks, particularly those aimed at managing high-order, nonlinear, and underactuated systems. Its study contributes not only to the theoretical advancement of control techniques but also to practical applications in robotics, automation, and aerospace systems where similar dynamic properties are prevalent.

SMC is a well-established robust control technique renowned for its effectiveness in handling uncertainties and nonlinearities in

dynamic systems. Recent advances have focused on improving SMC performance while mitigating inherent drawbacks such as chattering [5][6][7]. Owing to its robustness, SMC has been widely applied to the stabilization of underactuated mechanical systems, including the Rotary Inverted Pendulum (RIP) [8], Pendubot [9], and the Rotary Double Inverted Pendulum (RDIP) [10], with demonstrated effectiveness in both simulation studies and experimental implementations. Building on this foundation, the present work extends the application of SMC to a novel variant: the RPDIP, initially introduced in [11]. This configuration represents a structural enhancement of traditional RIP and RDIP systems, achieved by attaching a second pendulum in a parallel and symmetrical position relative to the first, mounted on the same rotating arm. While this design offers greater mechanical flexibility, it simultaneously introduces increased control complexity due to asymmetrical pendulum lengths and intensified nonlinear coupling.

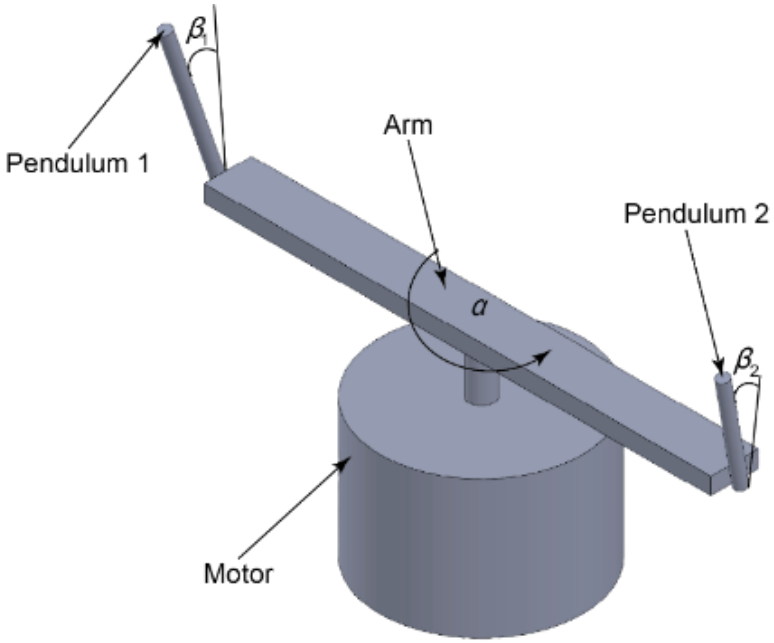

Fig. 1. The RPDIP configuration

Previous control strategies for the RPDIP have predominantly relied on Linear Quadratic Regulator (LQR) approaches [12][13], which may be insufficient under significant model uncertainties or external perturbations. In contrast, SMC offers inherent robustness and finite-time convergence, making it a promising candidate for this type of system [14]-[17]. A key aspect in SMC design is the formulation of an appropriate sliding surface, which directly influences system behavior and stability properties.

In this study, a linear sliding surface is constructed based on tracking error and its derivative, simplifying both analytical development and the practical implementation of the control law. The designed SMC ensures that the system trajectory converges to the sliding surface within a finite time and remains constrained to it thereafter, effectively mitigating the challenges posed by the system's nonlinear and coupled dynamics. Simulation results validate the control strategy by demonstrating convergence from perturbed initial conditions and sustained stability throughout the control process.

2. Dynamic Modeling of the System

2.1. Underlying Dynamics of the RPDIP System

The experimental platform, schematically depicted in Fig. 1, consists of a rigid iron base, a rotating arm actuated by a DC motor, and two pendulums mounted on opposing ends of the arm.

The system is equipped with dual rotary encoders for angular position measurement and feedback. Comprehensive physical specifications of the hardware components are listed in Table 1 [12], while key modeling parameters specific to the RPDIP configuration are presented in Table 2 [12].

The system under consideration is characterized by a set of fundamental mechanical and dynamical parameters. The mass of the i-th pendulum is represented as m_i in kilograms, and its length is denoted by l_i in meters. Its angular displacement is indicated by β_i in rad, and the corresponding moment of inertia is given as J_i in kgm^2. When accounting for angular configuration, the effective moment of inertia is calculated as $J_i = J_i \sin^2 \beta_i$.

The angular position of the rotating arm is represented by α in Rad, with length L (m), and rotational inertia designated as J_0 in kgm^2. Actuation is provided by a DC motor that generates a torque τ, measured in newton-meters (Nm). The gravitational acceleration constant g, m/s^2, is also integrated into the dynamic model.

To incorporate energy dissipation, viscous damping terms are introduced. The coefficient C_i corresponds to the *i*-th pendulum, while C_0 is associated with the rotating arm. Both coefficients are expressed in Nms, and they contribute significantly to capturing the resistance to motion in the system. These damping terms play an important role in accurately representing the dissipative effects and improving the realism of the dynamic model.

The dynamic behavior of the system is modeled using the Lagrangian formulation, which leads to the following expression:

$$L = T - V \tag{1}$$

The corresponding Euler–Lagrange equation is given by:

$$\frac{d}{dt}\frac{\partial L}{\partial \dot{q}_i} - \frac{\partial L}{\partial q_i} + \frac{\partial D}{\partial \dot{q}_i} = F_i \tag{2}$$

where

L : Lagrange function.

T : Kinetic energy of the system.

V : Potential energy of the system.

q_i : Generalized coordinate.

F_i : External force or moment.

D : Dissipated energy.

The kinetic energy of the system can be expressed as: (3)

$$T = \frac{1}{2}J_0\dot{\alpha}^2 + \frac{1}{2}J_1\dot{\beta}_1^{\,2} + \frac{1}{2}J_2\dot{\beta}_2^{\,2} + \frac{1}{2}m_1v_1^{\,2} + \frac{1}{2}m_2v_2^{\,2} \tag{3}$$

where v_1 and v_2 represent the linear velocities of the first and second pendulums, respectively.

Accordingly, the total kinetic energy of the system can be expressed in terms of these velocity components as:

$$\begin{aligned} T = {} & \frac{1}{2}J_0\dot{\alpha}^2 + \frac{1}{2}J_1\dot{\beta}_1^{\,2} + \frac{1}{2}J_2\dot{\beta}_2^{\,2} \\ & + \frac{1}{2}m_1(l_1\sin\beta_1\dot{\alpha})^2 + \frac{1}{2}m_1(L\dot{\alpha})^2 \\ & + \frac{1}{2}m_1(l_1\dot{\beta}_1)^2 - m_1l_1L\cos\beta_1\dot{\beta}_1\dot{\alpha} \\ & + \frac{1}{2}m_2(l_2\sin\beta_2\dot{\alpha})^2 + \frac{1}{2}m_2(L\dot{\alpha})^2 \\ & + \frac{1}{2}m_2(l_2\dot{\beta}_2)^2 - m_2l_2L\cos\beta_2\dot{\beta}_2\dot{\alpha} \end{aligned} \tag{4}$$

The potential energy of the system can be expressed as follows:

$$V = m_1gl_1\cos\beta_1 + m_2gl_2\cos\beta_2 \tag{5}$$

The energy dissipation caused by friction in the RPDIP system is represented by Equation (6) as follows:

$$D = \frac{1}{2}C_0\dot{\alpha}^2 + \frac{1}{2}C_1\dot{\beta}_1^{\,2} + \frac{1}{2}C_2\dot{\beta}_2^{\,2} \tag{6}$$

Based on the Lagrangian formulation, the

governing equations of motion are obtained in Equation (7) as follows:

$$\begin{aligned} L &= T - V \\ &= \frac{1}{2}J_0\dot{\alpha}^2 + \frac{1}{2}J_1\dot{\beta}_1^{\,2} + \frac{1}{2}J_2\dot{\beta}_2^{\,2} \\ &+ \frac{1}{2}m_1(l_1\sin\beta_1\dot{\alpha})^2 + \frac{1}{2}m_1(L\dot{\alpha})^2 \\ &+ \frac{1}{2}m_1(l_1\dot{\beta}_1)^2 - m_1l_1L\cos\beta_1\dot{\beta}_1\dot{\alpha} \\ &+ \frac{1}{2}m_2(l_2\sin\beta_2\dot{\alpha})^2 + \frac{1}{2}m_2(L\dot{\alpha})^2 \\ &+ \frac{1}{2}m_2(l_2\dot{\beta}_2)^2 - m_2l_2L\cos\beta_2\dot{\beta}_2\dot{\alpha} \\ &- m_1gl_1\cos\beta_1 - m_2gl_2\cos\beta_2 \end{aligned} \tag{7}$$

In the RDPIP system, actuation is achieved via a DC servo motor, whose torque-to-voltage relationship is characterized by the following expression:

$$\tau = \frac{K_m}{R_m}V_{In} - \frac{K_mK_t}{R_m}\dot{\alpha} \tag{8}$$

The dynamic equations of the RDPIP system are expressed in state-space form as follows:

$$\begin{bmatrix} P_{11} & P_{12} & P_{13} \\ P_{21} & P_{22} & P_{23} \\ P_{31} & P_{32} & P_{33} \end{bmatrix}\begin{bmatrix} \ddot{\alpha} \\ \ddot{\beta}_1 \\ \ddot{\beta}_2 \end{bmatrix} + \begin{bmatrix} Z_1 \\ Z_2 \\ Z_3 \end{bmatrix} = \frac{K_m}{R_m}\begin{bmatrix} V_{In} \\ 0 \\ 0 \end{bmatrix} \tag{9}$$

where

$P_{11} = J_0 + m_1l_1^{\,2}\sin^2\beta_1 + m_1L^2 + m_2l_2^{\,2}\sin^2\beta_2 + m_2L^2;$

$P_{12} = -m_1Ll_1\cos\beta_1;$

$P_{13} = -m_2Ll_2\cos\beta_2;$

$Z_1 = m_1l_1^{\,2}\dot{\beta}_1\dot{\alpha}\sin(2\beta_1) + m_1l_1L\dot{\beta}_1^{\,2}\sin\beta_1 + C_0\dot{\alpha}$

$+m_2l_2^{\,2}\dot{\beta}_2\dot{\alpha}\sin(2\beta_2) + (C_0 + K_mK_tR_m^{\,-1})\dot{\alpha};$

$P_{21} = -m_1Ll_1\cos\beta_1;$

$P_{22} = J_1 + m_1l_1^{\,2};$

$P_{23} = 0;$

$Z_2 = -m_1l_1^{\,2}\dot{\alpha}^2\sin\beta_1\cos\beta_1 - m_1gl_1\sin\beta_1 + C_1\dot{\beta}_1;$

$Z_2 = -m_1l_1^{\,2}\dot{\alpha}^2\sin\beta_1\cos\beta_1 - m_1gl_1\sin\beta_1 + C_1\dot{\beta}_1;$

$P_{31} = -m_2Ll_2\cos\beta_2;$

$P_{32} = 0;$

$P_{33} = J_2 + m_2l_2^{\,2};$

$Z_3 = -m_2l_2^{\,2}\dot{\alpha}^2\sin\beta_2\cos\beta_2 - m_2gl_2\sin\beta_2 + C_2\dot{\beta}_2.$

2.2. Linearized State-Space Representation of the RDPIP System

Linearization around the upright equilibrium configuration is essential for simplifying the analysis and enabling controller synthesis. By approximating the nonlinear dynamics in the vicinity of this operating point, the system can be represented by a linear model that facilitates analytical study and the design of conventional control strategies.

$$\begin{aligned} &\alpha \approx 0; \beta_1 \approx 0; \beta_2 \approx \pi \\ &\dot{\alpha} \approx 0; \dot{\beta}_1 \approx 0; \dot{\beta}_2 \approx 0 \end{aligned} \tag{10}$$

$$x = [\alpha \quad \beta_1 \quad \beta_2 \quad \dot{\alpha} \quad \dot{\beta}_1 \quad \dot{\beta}_2]^T \tag{11}$$

The linearized state-space representation, derived from the equilibrium configuration, is given as follows:

$$\begin{cases} \dot{x} = Ax + Bu \\ y = Cx \end{cases} \tag{12}$$

The computation of the state-space matrices A and B is based on the following formulations:

$$A = N^{-1}S; B = N^{-1}J \tag{13}$$

where

$$N = \begin{bmatrix} I_{3\times3} & & O_{3\times3} & \\ & J_0 + m_1L^2 & & \\ & +m_2L^2 & -m_1Ll_1 & -m_2Ll_2 \\ O_{3\times3} & -m_1Ll_1 & J_1 + m_1l_1^{\,2} & 0 \\ & -m_2Ll_2 & 0 & J_2 + m_2l_2^{\,2} \end{bmatrix} \tag{14}$$

$$S = \begin{bmatrix} & O_{3\times3} & & I_{3\times3} & & \\ & & & -(C_0 + \frac{K_mK_t}{R_m}) & 0 & 0 \\ 0 & 0 & 0 & & & \\ 0 & m_1gl_1 & 0 & 0 & -C_1 & 0 \\ 0 & 0 & m_2gl_2 & 0 & 0 & -C_2 \end{bmatrix} \tag{15}$$

$$J = \begin{bmatrix} 0 & 0 & 0 & 0 & \frac{K_m}{R_m} & 0 \end{bmatrix}^T \tag{16}$$

3. Linear sliding mode control

Linear Sliding Mode Control (LSMC)

represents a specific category within the broader SMC framework, wherein the sliding surface is defined as a linear combination of the system's state variables. This method retains the fundamental robustness and simplicity characteristic of traditional SMC while enhancing ease of implementation and analysis, particularly when applied to systems exhibiting linear or linearized dynamics [18]. The nonlinear system under consideration can be expressed as follows:

$$\dot{x} = f(x) + g(x)u \quad (17)$$

Let $x = \begin{bmatrix} x_1 & x_2 & \dots & x_n \end{bmatrix}^T$ denote the state vector of the system, where each x_i represents a state variable. The input U corresponds to the control signal applied to the system.

The analysis is conducted around the system's operating point, which is defined as follows:

Case 1: Mixed equilibrium configuration with the long pendulum upright and the short pendulum downward (see Fig. 2). The initial conditions are given in Equation (18) as follows:

$$\begin{cases} x_1 = 0; x_2 = 0; x_3 = \pi \\ x_3 = 0; x_4 = 0; x_5 = 0 \end{cases}; (x_0 = x) \quad (18)$$

Case 2: Mixed equilibrium configuration with the short pendulum upright and the long pendulum downward (see Fig. 3). The initial conditions are given in Equation (19) as follows:

$$\begin{cases} x_1 = 0; x_2 = \pi; x_3 = 0 \\ x_3 = 0; x_4 = 0; x_5 = 0 \end{cases}; (x_0 = x) \quad (19)$$

Case 3: Fully upright equilibrium configuration (see Fig. 4). The initial conditions are given in Equation (20) as follows:

$$\begin{cases} x_1 = 0; x_2 = 0; x_3 = 0 \\ x_3 = 0; x_4 = 0; x_5 = 0 \end{cases}; (x_0 = x) \quad (20)$$

If $U = 0$ then the system is balanced, and we can approximate the system in (1) to linear form.

$$\dot{x} = Ax + Bu \quad (21)$$

where

$$A = \left.\frac{\delta f}{\delta x}\right|_{\substack{x=x_0 \\ u=0}}; B = \left.\frac{\delta g}{\delta x}\right|_{\substack{x=x_0 \\ u=0}}$$

Fig. 2. Operating configuration of Case 1, where the long pendulum link is maintained at the upright equilibrium while the short pendulum link remains in the downward equilibrium position.

Fig. 3. Operating configuration of Case 2, where the short pendulum is stabilized at the upright equilibrium while the long pendulum remains at the downward equilibrium position.

Fig. 4. Case 3 corresponds to the fully upright equilibrium configuration, in which both the long and short pendulum links are aligned vertically upward.

Around the equilibrium point, the system's dynamics can be reasonably approximated as linear, thereby enabling the application of linear control design techniques.

The SMC strategy for the RDPIP system is developed utilizing the state-space formulation presented in Equation (11). The control objective is cast as a state-feedback problem, which facilitates the implementation of systematic control synthesis methods.

Subsequently, the linear sliding surface is constructed as follows:

$$S(x) = Ce \tag{22}$$

Where C is a constant row vector and e is the system state error vector. The control objective is to drive $S(x) \to 0$, thereby ensuring that the system remains on the sliding surface.

$$\dot{S}(x) = C\dot{x} = 0 \tag{23}$$

The equivalent control U_{EQ} is subsequently derived by setting the time derivative of the sliding surface to zero. This condition guarantees that, upon reaching the sliding manifold, the system trajectories remain confined to it during the sliding mode, thereby preserving the intended dynamic response.

$$U_{EQ} = -(CB)^{-1}CAx \tag{24}$$

To investigate the stability of the closed-loop system, Lyapunov's direct method is utilized. A Lyapunov candidate function is constructed based on the sliding surface $S(x)$, and is defined as follows:

$$V(s) = \frac{1}{2}S^2 \tag{25}$$

The proposed function is positive definite, as it satisfies $V(s) > 0$ for all $S \neq 0$ and $V(s) = 0$ when $S = 0$, thereby meeting the fundamental conditions of a Lyapunov candidate function.

The time derivative of the Lyapunov function $V(s)$ is computed as follows:

$$\dot{V}(s) = S\dot{S} \tag{26}$$

To guarantee that the system trajectories converge to and remain on the sliding surface, the Lyapunov function derivative $\dot{V}(s)$ must be negative definite, that is, $\dot{V}(s) < 0$ for all $S \neq 0$.

To satisfy this condition, the switching control term U_{SW} is introduced and defined using the sign function:

$$U_{SW} = -K\tanh(S) \tag{27}$$

Where $K > 0$ denotes the switching gain, and S refers to the standard tanh function, defined as follows:

$$\tanh(S)\begin{cases} \approx -1, \text{if } S \ll 0 \\ 0, \quad \text{if } S = 0 \\ \approx +1, , \text{if } S \gg 0 \end{cases} \tag{28}$$

By substituting this expression of U_{SW} into the overall control law and evaluating its influence

on $\dot{S}$, the following result is obtained:

$$\dot{V}(s) = S\dot{S} = -K|S| < 0;\ \forall S \neq 0 \quad (29)$$

This result verifies that the sliding surface exhibits both attractiveness and invariance, indicating that the system trajectories will converge to and persist on the sliding manifold. As a result, the closed-loop system achieves asymptotic stability in the Lyapunov sense, even in the presence of modeling uncertainties and external disturbances.

SMC comprises two main components: the equivalent control U_{EQ} and the switching control U_{SW}. The total control input applied to the system, denoted by U_{SMC}, is the sum of these two components and can be expressed as follows:

$$U_{SMC} = U_{EQ} + U_{SW} \quad (30)$$

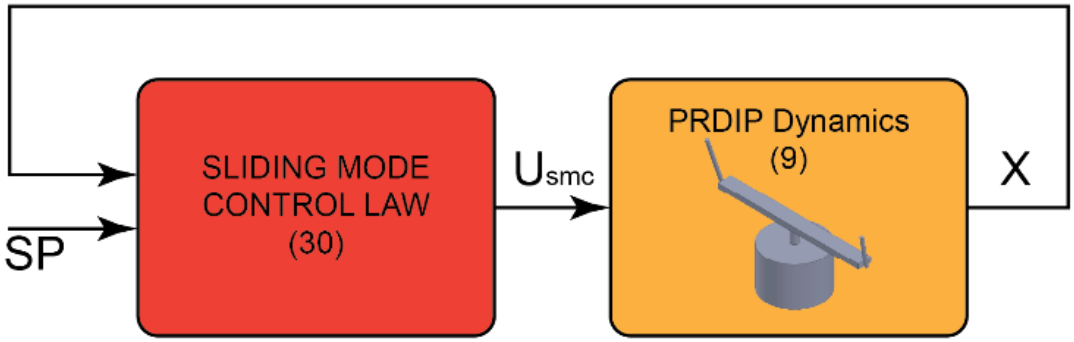

Fig. 5. Block diagram of the SMC-based control system for the RDPIP.

Fig. 5 illustrates the block diagram of the proposed control architecture based on the SMC strategy. The diagram shows the interaction between SMC control law (30) and the RPDIP plant dynamics described by Equation (9), forming a closed-loop control system. The controller receives the system states from the plant and computes the control input according to the SMC formulation. This architecture emphasizes the real-time nature of the SMC framework, where the controller continuously monitors deviations of the system states from the desired reference and generates a discontinuous control signal to compensate for disturbances and modeling uncertainties. The feedback loop is closed through real-time state measurements of the RPDIP system, allowing the controller to dynamically adjust the control input and maintain system stability.

4. Results and discussion

4.1. Simulation setup

Following the design of the control algorithm, a series of simulation experiments were performed within the MATLAB/Simulink platform to assess the performance and robustness of the proposed control approach. The dynamic behavior of the RDPIP system was modeled using experimentally derived motor and system parameters, as summarized in Tables 1 and 2. These parameters were instrumental in constructing a representative simulation model that closely reflects the actual system dynamics. To examine the controller's robustness, the simulations incorporated various disturbances and non-ideal initial conditions. Performance indicators, including settling time and overshoot, were systematically evaluated to confirm the system's stability and convergence characteristics.

In the simulation study, three distinct scenarios were examined to evaluate the controller's ability to regulate the pendulum from an initially deflected position to its target equilibrium state. For each scenario, specific values of the controller gains C and K were determined through a combination of trial-and-error tuning and optimization using the BAT algorithm [19][20]. These values were selected to achieve the desired dynamic response, reflecting performance criteria

in terms of stability, responsiveness, and damping characteristics.

Case 1: The pendulum is driven from the initial state $x_i = [0.02\ 0.01\ 3.128\ 0.0001\ 0.008\ 0.001]^T$ to the desired equilibrium position $x_i = [0\ 0\ \pi\ 0\ 0\ 0]^T$. The corresponding parameter values for matrices C and K are specified as follows.

$$C = [-17000\ 90000\ 10000\ -12000\ 13000\ 210]^T \quad (31)$$

$$K = 750 \quad (32)$$

Case 2: The pendulum is driven from the initial state $x_i = [0.02\ 3.128\ 0.01\ 0.0001\ 0.008\ 0.001]^T$ to the desired equilibrium position $x_i = [0\ \pi\ 0\ 0\ 0\ 0]^T$. The corresponding parameter values for matrices C and K are specified as follows.

$$C = [-17000\ 10000\ 90000\ -12000\ 210\ 13000]^T \quad (33)$$

$$K = 750 \quad (34)$$

Case 3: The pendulum is driven from the initial state $x_i = [0.02\ 0.01\ 0.01\ 0.0001\ 0.008\ 0.001]^T$ to the desired equilibrium position $x_i = [0\ 0\ 0\ 0\ 0\ 0]^T$. The corresponding parameter values for matrices C and K are specified as follows. (35)

$$C = [300\ 4130000\ -4202500\ 2000\ 199010\ -205750]^T$$

$$K = 130 \quad (36)$$

Table 1. System physical parameters

Parameter	Pendulum 1	Pendulum 2	The Arm
m_i	0.059	0.038	Na
l_i	0.127	0.082	Na
L	Na	Na	0.51
J_i	0.0001526	0.082	Na
J_0	Na	Na	0.75
c_i	1.526×10^{-4}	4.0693×10^{-4}	Na
c_0	Na	Na	4.978

Values of the DC motor are shown in Ref. [7]

Table 2. Physical parameters of the DC motor used for actuation

Parameters	Unit	Value
K_t	V / (rad / sec)	0.064944
K_b	V / (rad / sec)	0.064944
R_a	Ω	6.835271

4.2. Simulation results

The simulation results for Case 1 demonstrate the effectiveness and robustness of the proposed SMC strategy in stabilizing the rotary double inverted pendulum system. As illustrated in Fig. 6, the position responses of the arm and both pendulums exhibit rapid convergence to their respective desired equilibrium points. Specifically, the arm stabilizes at 0 rad with a maximum deviation of approximately 13×10^{-3} rad, while Pendulum 1 settles near 0 rad with transient oscillations remaining below 5×10^{-3} rad. Furthermore, Pendulum 2, starting from 3.128 rad, accurately converges to 3.141 rad with an undershoot of less than 0.01 rad. The corresponding velocity responses presented in Fig. 7 show that all angular velocities decay smoothly

to zero within approximately 5 seconds, with peak magnitudes not exceeding 0.25rad/s, reflecting favorable damping behavior and dynamic stability. Additionally, the control input and sliding surface shown in Fig. 8 confirm that the control signal U_{smc} remains bounded within $\pm 12V$. The sliding surface S rapidly converges to and maintains a value of zero, indicating that the system has successfully reached and remained on the sliding manifold.

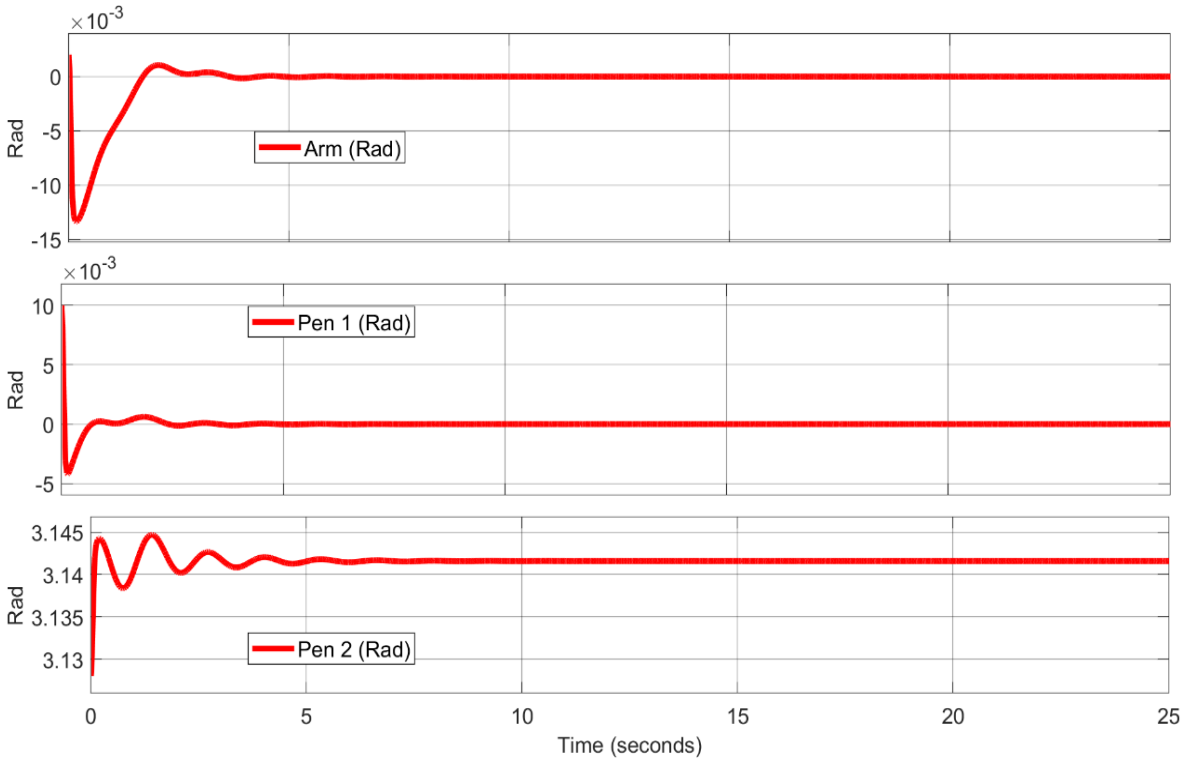

Fig. 6. Position of the arm and two pendulums

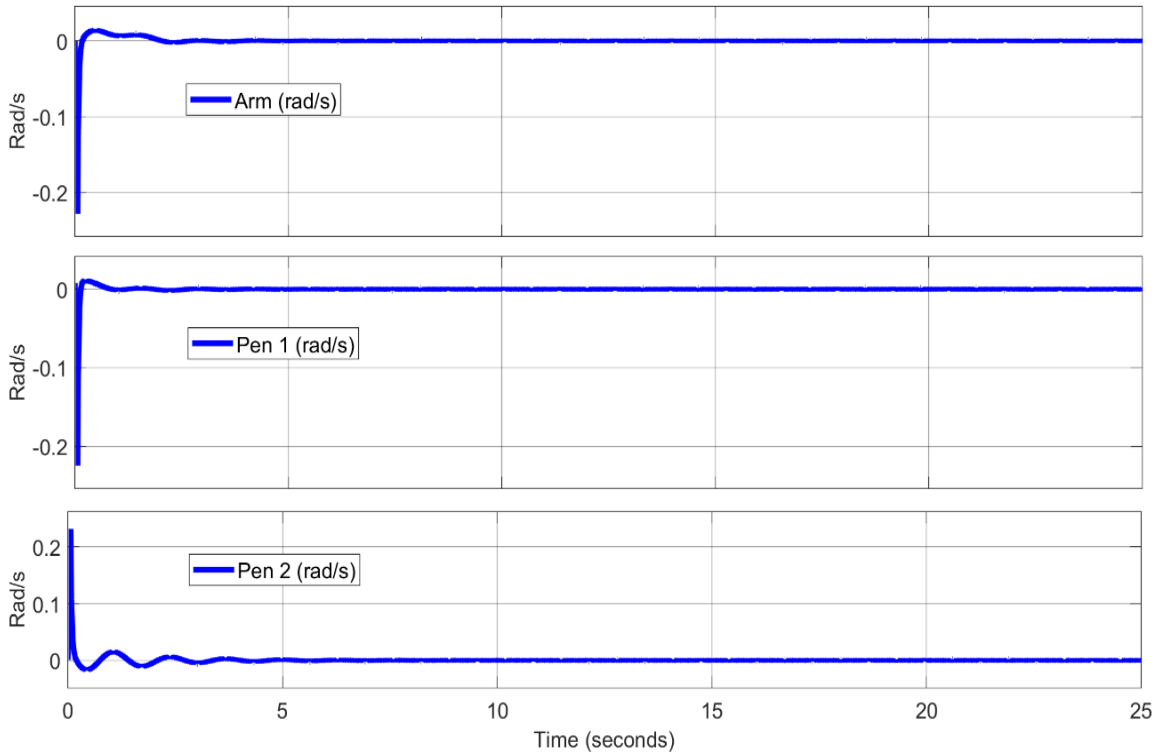

Fig. 7. Velocity of the arm and the two pendulums

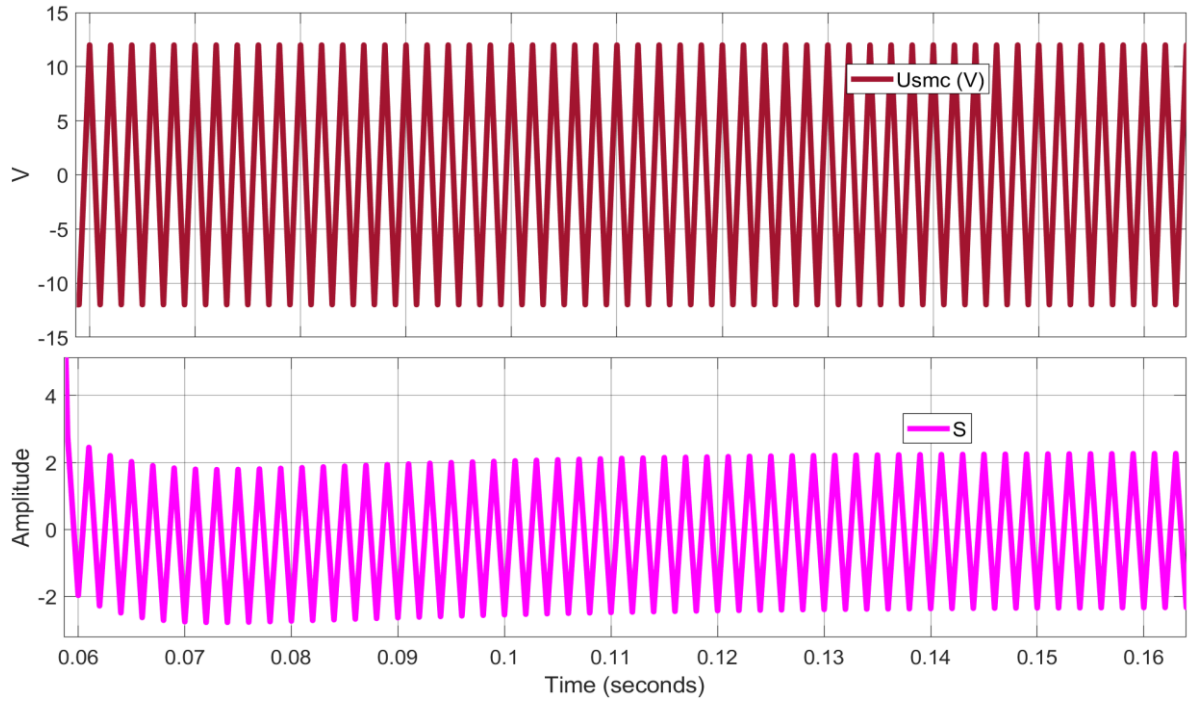

Fig. 8. Control signal and sliding surface

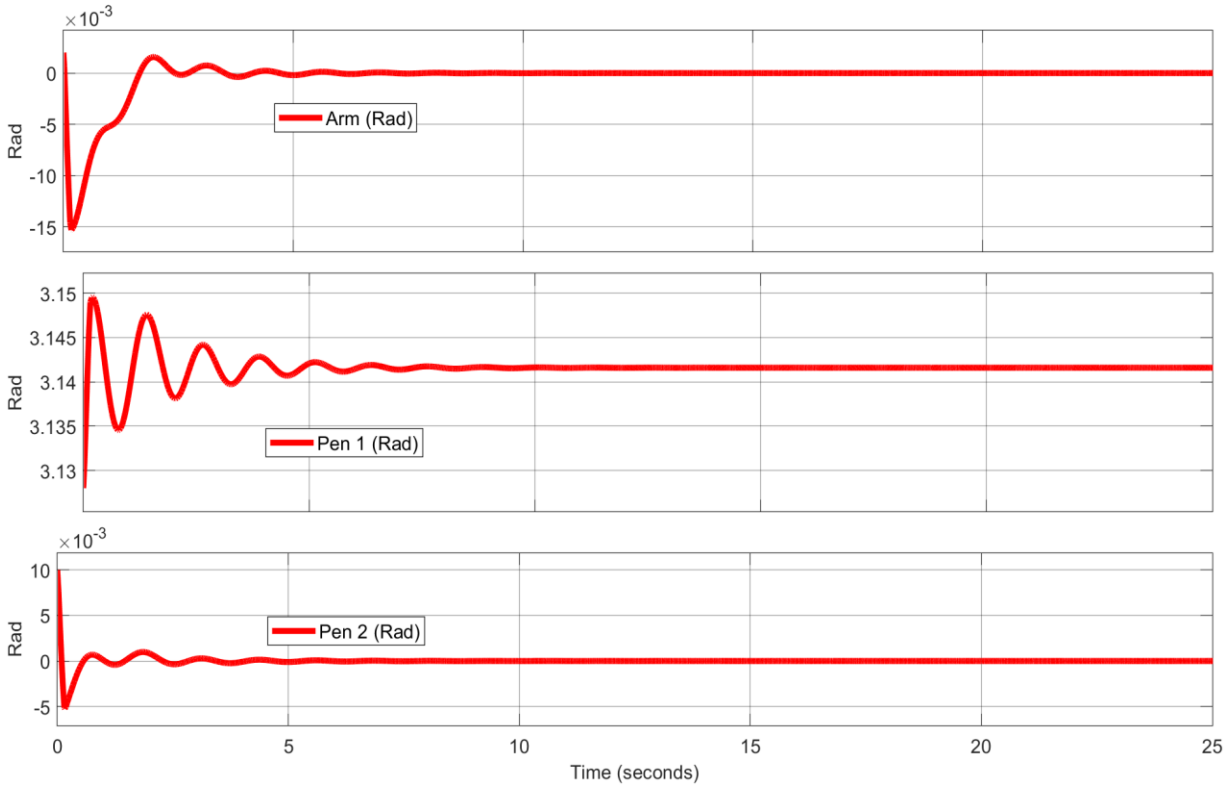

Fig. 9. Position of the arms and two pendulums

To evaluate the controller's flexibility, Case 2 was conducted under modified initial conditions, which reaffirmed the high adaptability of the proposed SMC algorithm. The results in Fig. 9 demonstrate a seamless convergence of the arm and Pendulum 2 positions toward the origin, while Pendulum 1, initiated at 3.128rad, achieves a stable equilibrium at 3.141rad with transient oscillations effectively suppressed below the 5 x 10^{-3}rad threshold. Concurrently, the angular velocity responses in Fig. 10 illustrate optimal damping characteristics, as all state variables settle to zero within 5 seconds with peak magnitudes not exceeding 0.2rad/s. System

stability is further corroborated by the control signal in Fig. 11, which remains within the ±12V limit, while the sliding surface S rapidly approaches and maintains a zero value, confirming the successful establishment and robust maintenance of the sliding mode.

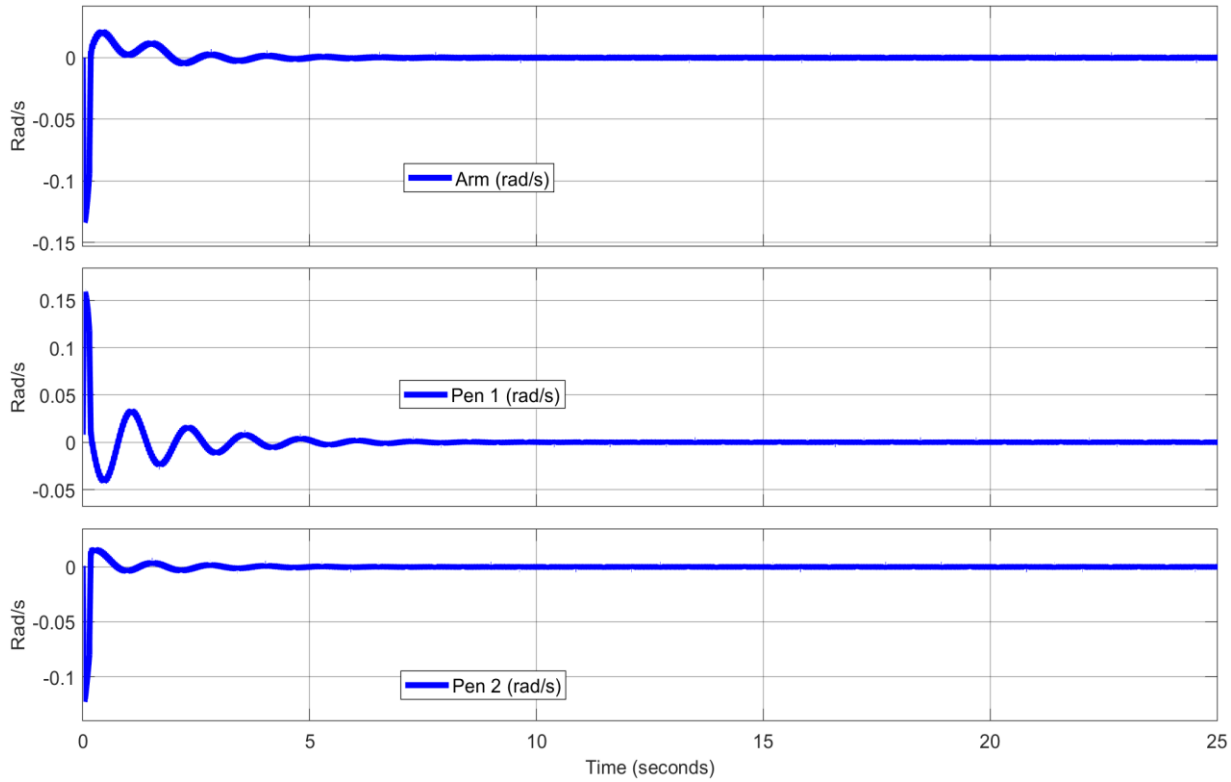

Fig. 10. Velocity of the arm and the two pendulums

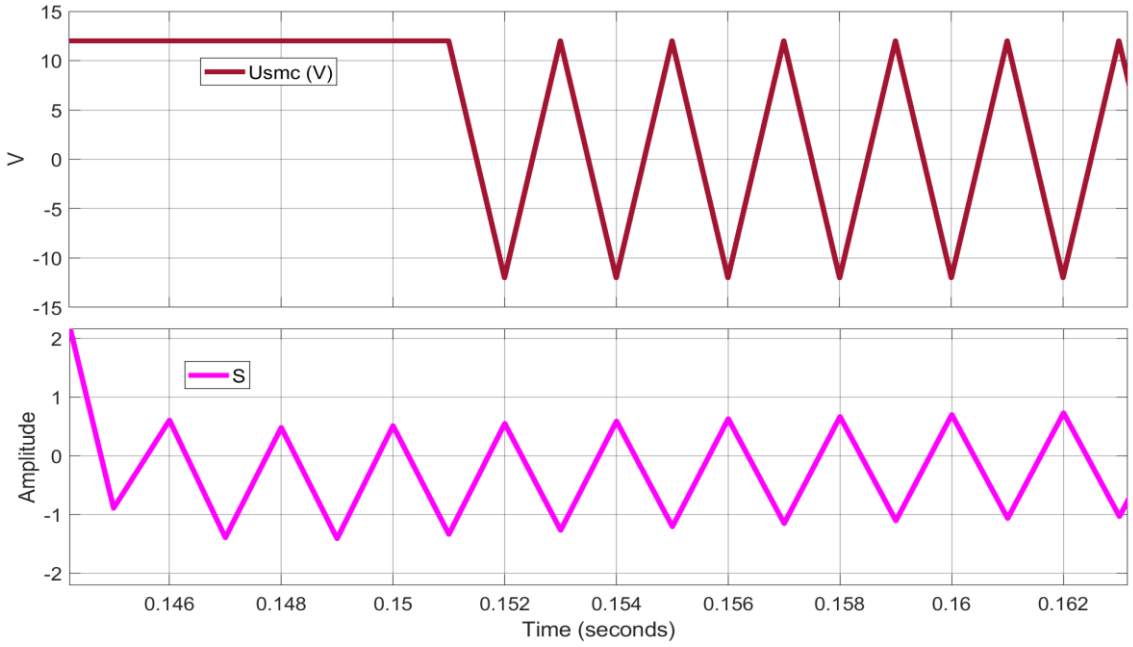

Fig. 11. Control signal and sliding surface

Case 3 serves to investigate the operational constraints of the control strategy under more rigorous initial conditions, revealing intensified dynamical complexities. As illustrated in Fig. 12, the position responses exhibit retarded convergence rates alongside pronounced overshoot, with the arm position peaking at 0.4rad before stabilizing, while the pendulums undergo oscillations within a ±0.012rad margin. The elevated transient energy is further evidenced in

Fig. 13, where angular velocity variables require approximately 10 seconds to settle with peak magnitudes approaching 0.2rad/s. Although the control input is maintained within the ±12V boundary, the analysis of Fig. 14 confirms that the sliding surface S fails to achieve zero-convergence and instead displays persistent oscillations, highlighting the compromised robustness of the sliding mode when subjected to high-demand operational scenarios.

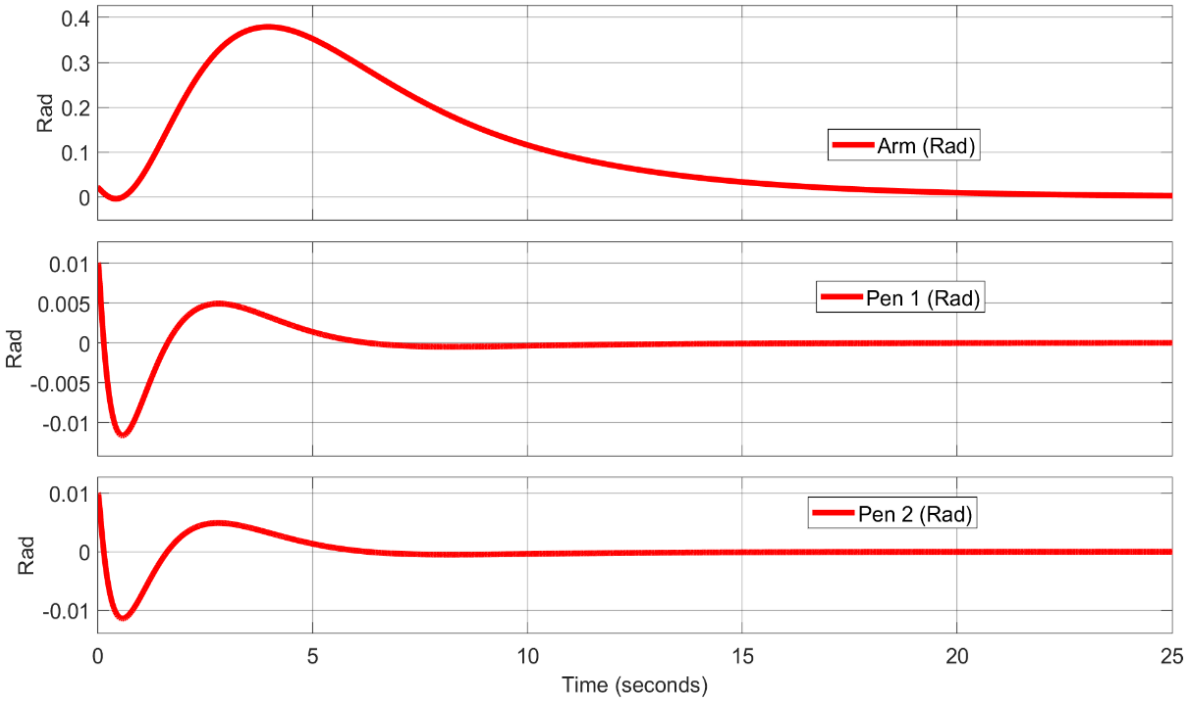

Fig. 12. Position of the arms and two pendulums

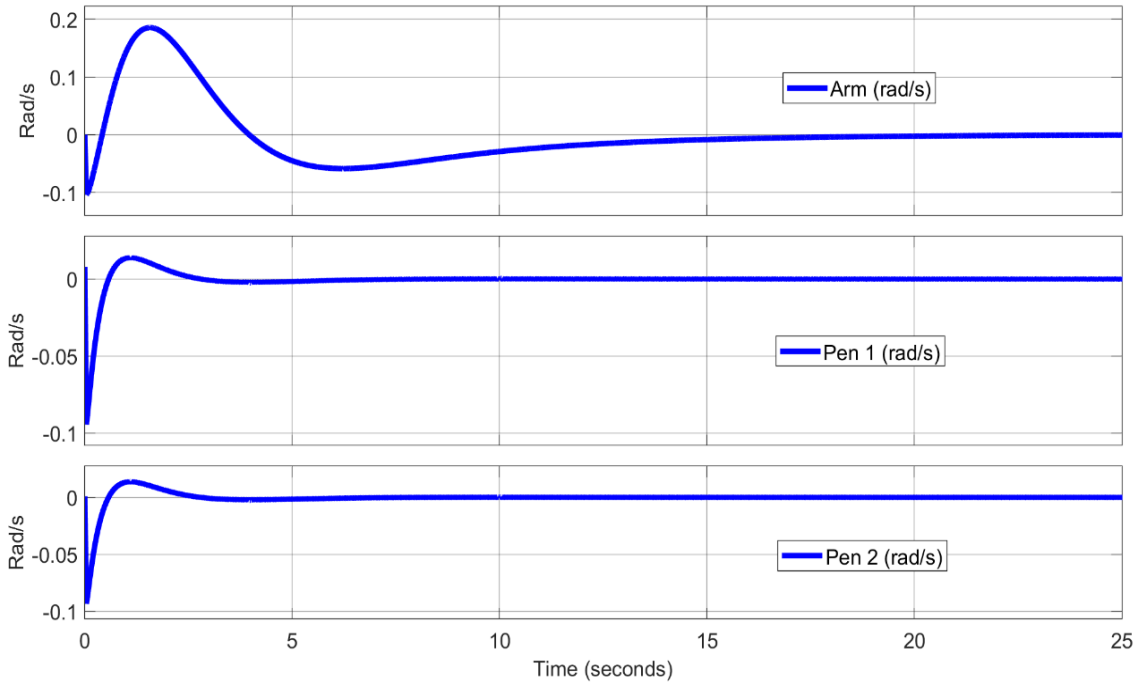

Fig. 13. Velocity of the arm and the two pendulums

To quantitatively assess the control performance, the root mean square error (RMSE) was employed as a metric for both position and velocity tracking. RMSE is computed as.

$$\mathrm{RMSE} = \sqrt{\frac{1}{N}\sum_{i=1}^{N}(x_i - x_d)^2} \quad (37)$$

where x_i denotes the measured value at the i^{th}

sample, x_d is the desired reference value, and N is the total number of samples.

The desired equilibrium configurations for the three test cases are specified in (18), (19), and (20), whereas the corresponding RMSE results are presented in Table 3 as follows:

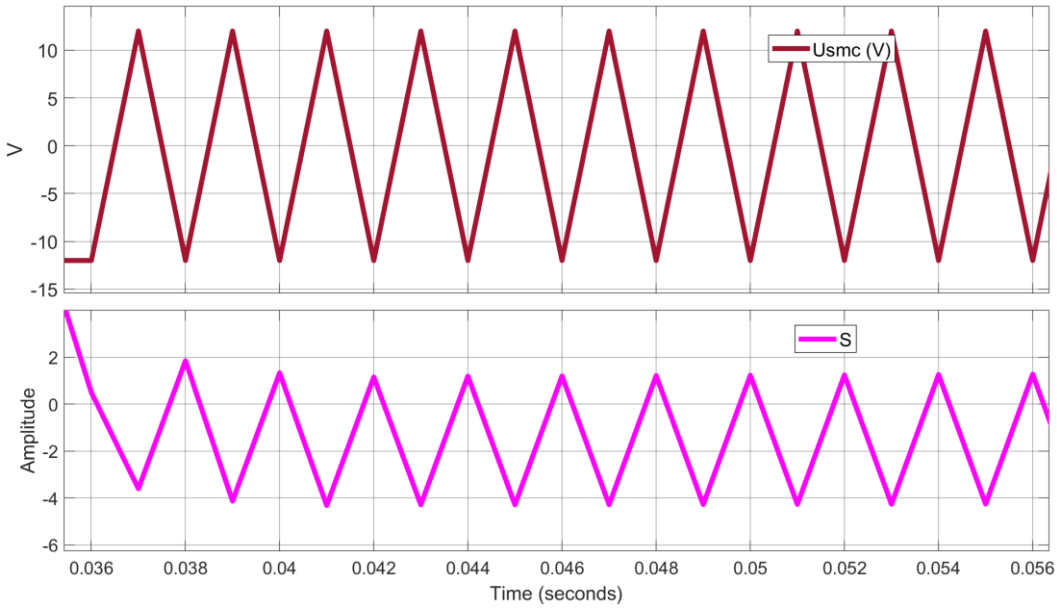

Fig. 14. Control signal and sliding surface

Table 3. RMSE error values for cases

Case	RMSE
1	0.001312
2	0.001555
3	0.000196

As presented in Table 3, the RMSE error values obtained for all test cases are consistently low, highlighting the accuracy of the proposed control approach in both position and velocity tracking. The relatively small magnitudes of the errors indicate that the system is able to closely follow the desired reference trajectories without significant deviations.

This outcome demonstrates not only the effectiveness of the method in minimizing steady-state error but also its robustness in maintaining reliable performance across different equilibrium configurations. Consequently, these results validate the suitability of the proposed strategy for practical implementation in scenarios that demand high-precision control.

4.3. Experimental setup

To validate the proposed control scheme in a real-time environment, the RPDIP system was designed using SolidWorks software, as illustrated in Fig. 15, and physically constructed on a custom hardware platform, as shown in Fig. 16. The experimental setup consists of the following main components:

1.STM32F407 microcontroller.

2.Nisca NF5475 DC motor with an integrated encoder.

3. H-bridge driver circuit.

4.Two incremental encoders.

5.CP2102 USB-to-TTL serial converter.

6.Rotary arm structure.

7.Two pendulum links.

This hardware configuration enables closed-loop experimental validation of the proposed control algorithms, effectively bridging the gap between simulation and real-world implementation. The control logic is developed and deployed using MATLAB/Simulink, which interfaces directly with the STM32F407 microcontroller for real-time execution. Experimental data are captured during operation and subsequently processed and

visualized using Python scripts executed within the Visual Studio Code environment. This integration ensures a seamless workflow from controller design to experimental analysis.

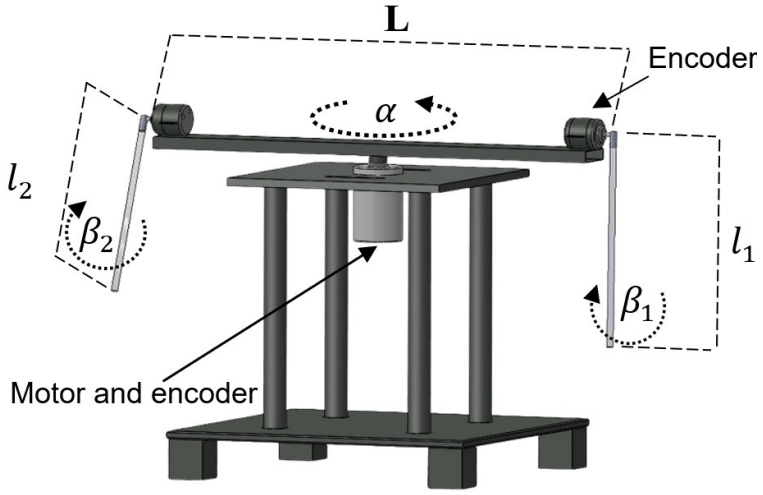

Fig. 15. SolidWorks model of the RDPIP system [12]

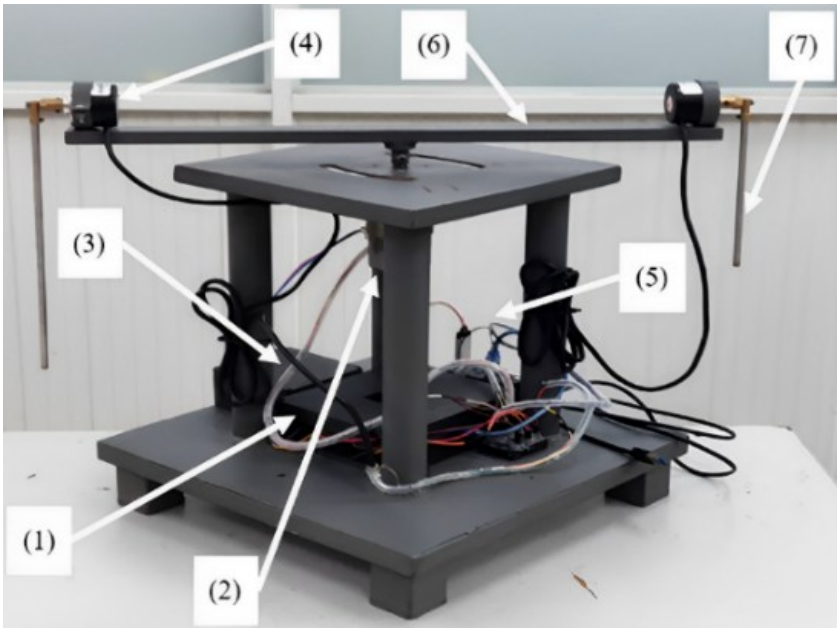

Fig. 16. RDPIP hardware setup [13]

4.4. Experimental results

The physical parameters employed in the experimental setup are identical to those used in simulation studies, and the test cases directly correspond to those defined in the simulation environment. In Case 1, the desired equilibrium state is defined as $x_i = [0\ 0\ \pi\ 0\ 0\ 0]^T$. The experimental results, as illustrated in Fig. 17, Fig. 18, and Fig. 19, show that Pendulum 1 transitions from an initial angle of approximately 3.1rad to 0rad and remains stable. Pendulum 2 oscillates around the target position of π rad, staying relatively close to the desired value. The swing arm exhibits continuous oscillation around the setpoint, however, its trajectory remains confined within acceptable bounds. The velocity feedback contains high-frequency, large-amplitude noise, particularly in Pendulum 1. The control signal U_{SMC} reaches the saturation limit of $\pm$12V with rapid switching, while the sliding surface S oscillates around zero. Although the system does not achieve the ideal stability observed in simulation, the experimental outcomes still demonstrate the controller's ability to regulate the system and maintain its behavior near

the desired state.

In Case 2, the desired equilibrium state is defined as $x_i = [0\ \pi\ 0\ 0\ 0\ 0]^T$. As shown in Fig. 20, Fig. 21, and Fig. 22, the experimental results indicate that Pendulum 2 successfully stabilizes near 0rad, while Pendulum 1 oscillates around the target value of π rad with small deviations. The swing arm exhibits continuous oscillation with a peak amplitude of approximately 0.9rad near the setpoint, however, its trajectory remains within the allowable operating limits. The velocity responses demonstrate noticeable noise and rapid switching, particularly for the arm and Pendulum 1, although the system maintains bounded behavior. The control signal U_{SMC} reaches saturation at $\pm$12V and exhibits frequent switching, while the sliding surface S fluctuates around zero but does not fully converge. Although the system does not achieve ideal convergence as in the simulation, the overall behavior remains stable and demonstrates the controller's ability to regulate the system close to the desired equilibrium. Minor tuning of gain matrices and signal filtering may further improve performance in future trials.

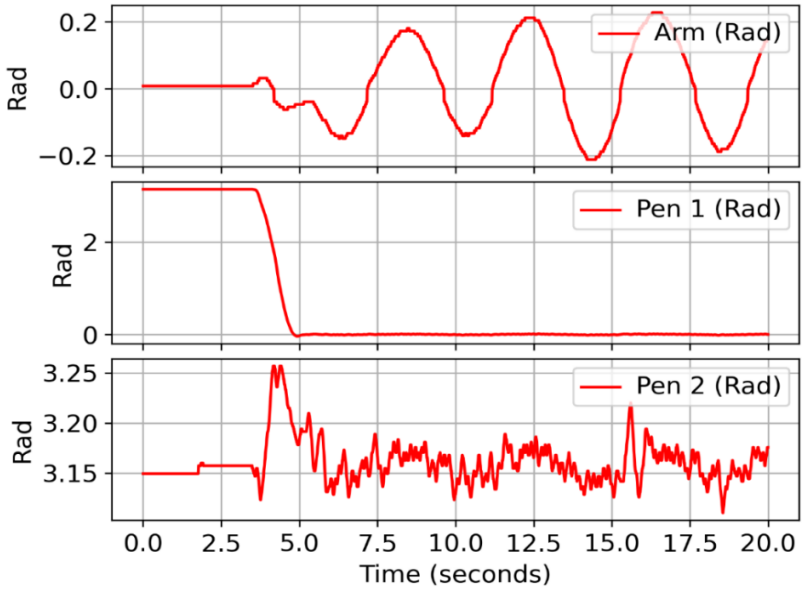

Fig. 17. Position of the arms and two pendulums

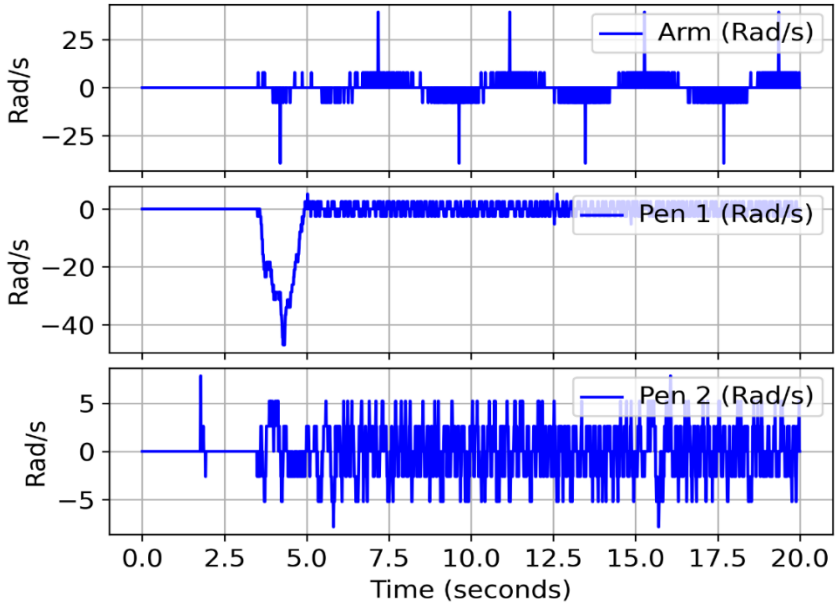

Fig. 18. Velocity of the arm and the two pendulums

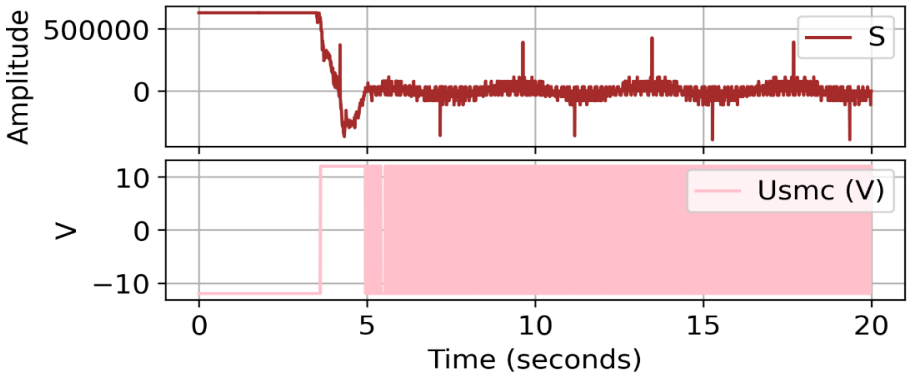

Fig. 19. Sliding surface and control signal

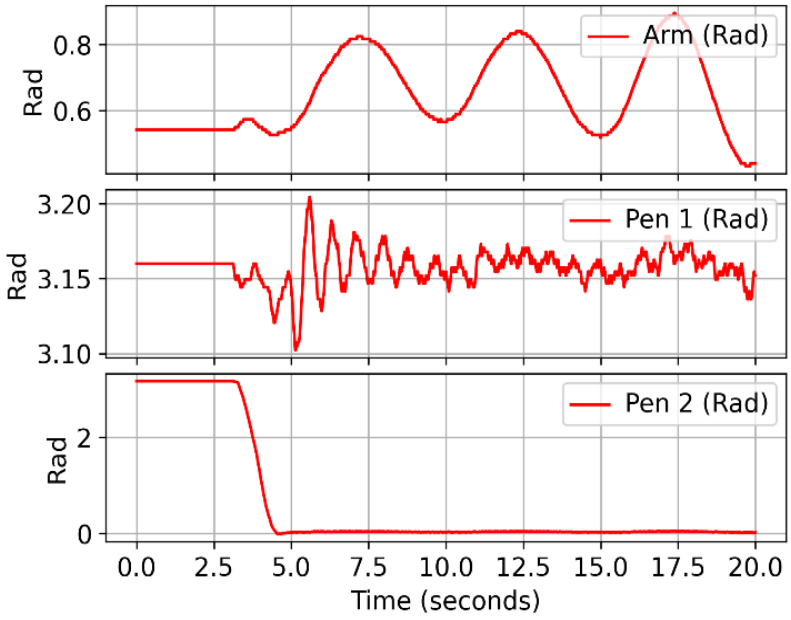

Fig. 20. Position of the arms and two pendulums

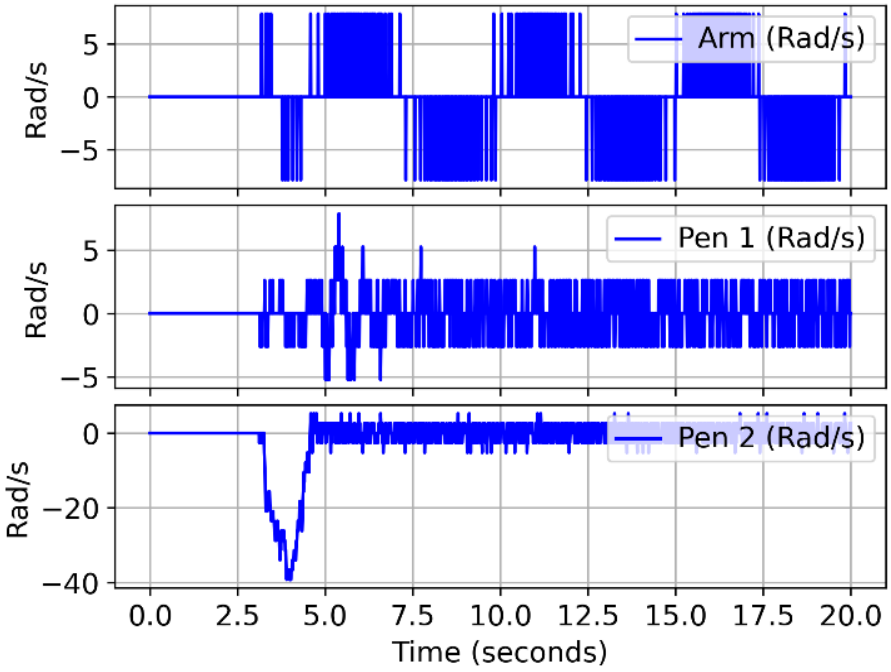

Fig. 21. Velocity of the arm and the two pendulums

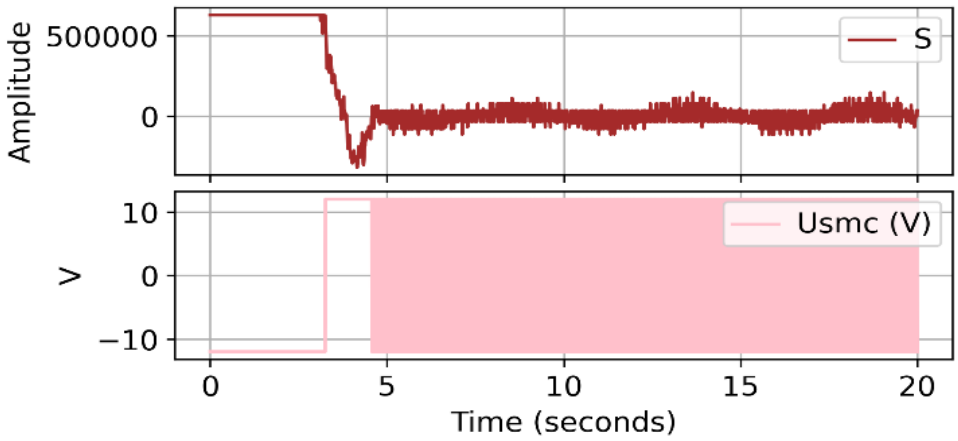

Fig. 22. Sliding surface and control signal

In Case 3, the desired equilibrium state is defined by $x_i = [0\ 0\ 0\ 0\ 0\ 0]^T$, which serves as the target for system regulation. In this case, multiple experimental trials were conducted using various combinations of the augmentation matrices C and K. However, the experimental outcomes did not achieve the same level of success as observed in the simulation results, which may be attributed to the increased sensitivity of the physical system and implementation uncertainties under real-world conditions. To address these limitations, future work will focus on incorporating disturbance observation techniques and integrating adaptive control algorithms to enhance robustness and performance.

5. Conclusion

This paper presented a SMC strategy to stabilize the RPDIP, a complex and underactuated nonlinear system. A linear sliding surface was designed to simplify implementation while preserving the robustness properties of classical SMC. Through Lyapunov-based analysis, the stability of the closed-loop system was theoretically guaranteed.

Simulation results across three distinct initial conditions confirmed the controller's effectiveness. In all cases, the system exhibited rapid convergence, limited overshoot, and smooth velocity decay. Notably, Case 3, which involved a more challenging initial condition, still achieved successful stabilization in simulation, thereby demonstrating the strong robustness and adaptability of the proposed control strategy.

However, experimental validation revealed some limitations. While Cases 1 and 2 showed reasonable performance under real-world conditions, Case 3 failed to reproduce the same level of success as in the simulation. The system exhibited sustained oscillations, and the sliding surface did not converge as expected. These issues likely stem from hardware non-idealities, unmodeled dynamics, high-frequency noise in velocity feedback, and actuator saturation. Additionally, the control input exhibited high-frequency switching (chattering), which may degrade hardware lifespan and energy efficiency.

Future improvements will include the integration of adaptive or higher-order SMC algorithms to reduce chattering and enhance robustness against physical uncertainties. The use of disturbance observers and signal filtering will also be investigated to improve measurement quality and real-time control accuracy. Moreover, the development and implementation of a fuzzy SMC framework will be explored as a promising direction for further system enhancement [9].

Supplementary materials

The experimental demonstration of this work can be viewed at the following link: https://www.youtube.com/watch?v=exxsNAtzSF4

References

[1]. C. Ekaputri, A. Syaichu-Rohman. (2012).

Implementation model predictive control (MPC) algorithm-3 for inverted pendulum. *2012 IEEE Control and System Graduate Research Colloquium*, *pp. 116-122*. doi: 10.1109/ICSGRC.2012.6287146

[2]. W. Linglin, L. Yongxin, Z. Xiaoke. (2015). Design of reinforce learning control algorithm and verified in inverted pendulum. *2015 34th Chinese Control Conference (CCC), pp. 3164-3168*. doi: 10.1109/ChiCC.2015.7260128

[3]. N. Bordoloi, M. Buragohain. (2017). Bacteria foraging optimized and modified PSO optimized PD-SMC and PID-SMC controller for inverted pendulum system. *2017 International Conference on Smart grids, Power and Advanced Control Engineering (ICSPACE), pp. 171-176*. doi: 10.1109/ICSPACE.2017.8343424

[4]. M.-T. Vo, H.-N. Duong, V.-H. Nguyen. (2024). Comparative Study of Swing-Up Controllers: Passivity-Based Swing-Up Control and Sliding Mode Technique Combined Energy-Based Method for Rotational Inverted Pendulum System. *2024 9th International Conference on Applying New Technology in Green Buildings (ATiGB), IEEE, pp. 218-223*. doi: 10.1109/ATiGB63471.2024.10717747

[5]. L.P.T. Nguyen, T.T. Tran. (2023). A Family of Sliding Mode Controllers: Analysis, Design and Comparison. *2023 International Conference on System Science and Engineering (ICSSE), pp. 462-467*. doi: 10.1109/ICSSE58758.2023.10227176

[6]. T.T. Tuyen, J. Yang, L. Liao, N.G.M. Thao. (2025). Recent Advances in Sliding Mode Control Techniques for Permanent Magnet Synchronous Motor Drives. *Electronics*, 14(19), 3933. doi: 10.3390/electronics14193933

[7]. T.T. Tran, V.H. Nguyen. (2021). A Novel Design of Chattering-free Sliding Mode Control for a Nonlinear Dynamic System. *2021 4th International Conference on Robotics, Control and Automation Engineering (RCAE)*, pp. 213-217. doi: 10.1109/RCAE53607.2021.9638929

[8]. M.A. Khanesar, M. Teshnehlab, M.A. Shoorehdeli. (2007). Sliding mode control of Rotary Inverted Pendulm. *2007 Mediterranean Conference on Control & Automation*, *pp. 1-6*. doi: 10.1109/MED.2007.4433653

[9]. M.-D. Tran, M.-T. Vo, V.-D.-H. Nguyen. (2023). A comparative study between sliding mode and fuzzy sliding mode control for pendubot. *Serbian Journal of Electrical Engineering*, 20(3), 361-390. doi: 10.2298/SJEE2303361T

[10]. S. Singh, A. Swarup. (2021). Control of Rotary Double Inverted Pendulum using Sliding Mode Controller. *2021 International Conference on Intelligent Technologies (CONIT), pp. 1-6*. doi: 10.1109/CONIT51480.2021.9498525

[11]. H.D. Khoi. (2013). Using LQR Algorithm to Control Circular Two Stage Parallel Inverted Pendulum System. *Journal of Engineering, National Ilan University*, (9), 101-114. https://doi.org/10.6176/BCE.2013.09.17

[12]. M.-D. Vo et al. (2023). Linear Quadratic Regulators Optimal Control of Rotary Double Parallel Inverted Pendulum. *2023 International Conference on Control, Robotics and Informatics (ICCRI), pp. 14-18*. https://doi.org/10.1109/ICCRI58865.2023.00009

[13]. M.-T. Vo et al. (2024). Development and Control of Underactuated Parallel Rotary Double Inverted Pendulum System. *Proceedings of the 12th International Conference on Robotics, Vision, Signal Processing and Power Applications, pp.239-246. RoViSP 2021. Lecture Notes in Electrical Engineering, vol 1123. Springer*. https://doi.org/10.1007/978-981-99-9005-4_30

[14]. S. Tokat, M.S. Fadali, O. Eray. (2015). A Classification and Overview of Sliding Mode Controller Sliding Surface Design Methods. *Recent Advances in Sliding Modes: From Control to Intelligent Mechatronics. Studies in Systems, Decision and Control, vol 24. Springer*. https://doi.org/10.1007/978-3-319-

18290-2_20

[15]. D. Qian, J. Yi, D. Zhao. (2008). Hierarchical sliding mode control for a class of SIMO under-actuated systems. *Control and Cybernetics*, 37(1), 159-175. 10.1504/IJMIC.2011.041779

[16]. J.-X. Xu, Z.-Q. Guo, T.H. Lee. (2012). Sliding mode controller design for underactuated systems. *2012 12th International Workshop on Variable Structure Systems, pp. 385-390*. doi: 10.1109/VSS.2012.6163533

[17]. W. Perruquetti, J.-P. Barbot. (2002). Sliding Mode Control in Engineering (1st ed.). *CRC Press*.https://doi.org/10.1201/9780203910856

[18]. K. Sugawara, M. Izutsu, S. Hatakeyama, M. Iwase. (2014). Stabilization of Triple Furuta pendulum by sliding mode control. *IECON 2014 - 40th Annual Conference of the IEEE Industrial Electronics Society, pp. 2872-2877*. doi: 10.1109/IECON.2014.7048916

[19]. M.O. Okwu, L.K. Tartibu. (2021). Bat Algorithm. Metaheuristic Optimization: Nature-Inspired Algorithms Swarm and Computational Intelligence, Theory and Applications. *Studies in Computational Intelligence, (SCI, vol 927). Springer*. https://doi.org/10.1007/978-3-030-611118_8

[20]. T.-T.-D. Le. (2025). LQR Controller Based on BAT Algorithm for Rotary Double Parallel Inverted Pendulum. J Fuzzy Syst Control, 3(2), 112-121. https://doi.org/10.59247/jfsc.v3i2.304